A sea ice concentration estimation algorithm utilizing radiometer and SAR data

Finnish Meteorological Institute (FMI), Helsinki, PB 503, 00101, Finland

Correspondence to: J. Karvonen (juha.karvonen@fmi.fi)

Abstract

abstr We have studied the possibility of combining the high-resolution SAR segmentation and ice concentration estimated by radiometer brightness temperatures. Here we present an algorithm for mapping a radiometer-based concentration value for each Synthetic Aperture Radar (SAR) segment. The concentrations are estimated by a Multi-Layer Perceptron (MLP) neural network which has the AMSR-2 (Advanced Microwave Scanning Radiometer 2) radiometer polarization ratios and gradient ratios of four radiometer channels as its inputs. The results have been compared numerically to the gridded Finnish Meteorological Institute (FMI) ice chart concentrations and high-resolution AMSR-2 ASI algorithm concentrations provided by University of Hamburg and also visually to the AMSR-2 bootstrap algorithm concentrations, which are given in much coarser resolution. The differences when compared to FMI daily ice charts were on average small.

1 Introduction

intro

Ice concentration is defined as the ratio of the ice covered area to the total area for a given sea region. From this definition directly follows that ice concentration is dependent on the resolution of the measurement. This fact also complicates direct comparison to different ice concentration products in different resolutions. Space-borne radiometers are an important data source capable of estimating the ice concentration in a resolution of around 10 km or even coarser. Also other space-borne instruments for estimating the ice concentration have been used. The advantage of radiometer platforms and the radiometer instruments on-board, like AMSR-2 (Advanced Microwave Scanning Radiometer 2) is that their orbit and wide swaths enable a daily coverage over most of the ice-covered sea areas. Algorithms producing ice concentration from radiometer data are e.g. the NASA team algorithm (Cavalieri et al., 1984), the bootstrap algorithm (Comiso, 1986, 1995) used by the National Sea Ice Data Center (NSIDC), and the Artist Sea Ice (ASI) algorithm (Kaleschke et al., 2001; Spreen et al., 2008) of University of Bremen (UB).

The ASI algorithm utilizing the full resolution of the AMSR-2 has been introduced and is operationally providing Arctic and Antarctic ice concentration at University of Hamburg (UH) (Beitsch et al., 2013; Beitsch and Kaleschke, 2014). Here we also provide a comparison of our results to these fine-resolution radiometer ice concentration estimates. Ice concentration in a finer resolution can also be retrieved from instruments capable of measuring surface temperature, but these instruments operate at (infrared) wavelengths not penetrating the cloud cover. Due to relatively long cloudy periods, which can last even several weeks, during the wintertime there can occur long temporal gaps in these measurements. One example of such algorithms is the MPA (MODIS potential open water algorithm) (Drüe and Heinemann, 2004), developed at University of Bonn, using the Moderate Resolution Imaging Spectroradiometer (MODIS) instrument data for ice concentration retrieval. Synthetic aperture radar (SAR) data, with high resolution, large spatial coverage and capability to acquire data through cloud cover, have not yet widely been used in measuring sea ice concentration. Some studies using single-band SAR for estimation of ice concentration have however been made, e.g. those reported in (Bovith and Andersen, 2005; Berg, 2011; Karvonen, 2012; Karvonen et al., 2012). Automated sea ice classification schemes, which implicitly include ice concentration or an open water class, based on single-band and dual-band SAR texture and backscattering have also been proposed, e.g. in (Clausi and Jernigan, 2000; Clausi, 2001; Deng and Clausi, 2004, 2005; Maillard et al., 2005; Yu and Clausi, 2007; Ochilov and Clausi, 2012; Leigh et al., 2014). These methods use multiple techniques, like the gray-level co-occurrence texture features (Haralick at al., 1973), Markov random fields (MRF) (Rue and Held, 2005), and Gabor filters (Pichler et al., 1996; Clausi and Jernigan, 2000) for classifying the sea ice SAR data. Dokken (Dokken et al., 2000) developed a SAR ice concentration algorithm which is a combination of mean ratio (relating average SAR backscatter to typical open water and sea ice values), a local threshold and a wavelet method (to detect edges around ice floes) for RADARSAT-1 and ERS SAR imagery. It has also been shown that using dual-polarized C-band SAR data (HH/HV) improves the ice concentration estimation compared to single-channel SAR (HH) (Karvonen, 2014). A method for ice classification into four ice classes and open water by combining SSM/I radiometer ice concentration and SAR data was introduced in (Kaleschke and Kern, 2000). Here we propose a novel method

3

combining high-resolution SAR image segmentation and the lower-resolution radiometer ice concentration estimation to yield ice concentration estimates with improved areal boundaries defined by the SAR resolution. The algorithm is based on SAR image segmentation and on multi-layer perceptron (MLP) neural network.

2 Study area, time and data

We studied our novel algorithm over the Baltic Sea. The study area defined by the upper left and lower right corner was from (56.0° N, 16.0° E) to (66.0° N, 31.0° E). The areas is shown in Fig. 1. The area of the Baltic Sea is 422000 km². The Baltic Sea ice cover has large annual and local variations. Annual maximum ice extent varies between 52000 km² 422000 km², average being 218000km² (reached in January-March). Bay of Bothnia and Gulf of Finland have at least partial ice cover every year. The Baltic Sea ice is moving and the ice concentration is changing during each winter, also some melting can occur even in the mid-winter, because the temperature may also vary from -40 C^o to +10 C^o even during the mid-winter. Only the land fast ice areas covering a relatively narrow zone along the coasts (from a few kilometers to a few tens of kilometers) remain stable and typically have a high concentration throughout the winter. Winter 2013-2014 was a mild ice winter in the Baltic, and also the air temperature was varying from cold to warm (above zero) many times during the winter.

The radiometer data were AMSR-2 radiometer level 1R brightness temperature data Maeda (2013). The SAR data were dual-polarized (HH/HV polarization combination) RADARSAT-2 ScanSAR Wide mode data. In this study we only utilized the HH channel of the SAR data. The SAR mosaics were georectified to Mercator projection, and an incidence angle correction was applied to each SAR image included in the mosaic. The ice concentration estimates were also produced in Mercator projection, mapped and re-sampled to the resolution of 500 m, which corresponds to the projection and resolution of our SAR mosaics. In the projection we used the WGS84 datum, and the reference latitude (true scale latitude) was 61 degrees 40 minutes (northern). The data set was divided into a training data set, consisting of daily SAR mosaics and AMSR-2 brightness temperature mosaics from 23 January 2014 to 1 February 2014, and a

4

test data set, consisting of daily SAR mosaics and the corresponding daily AMSR-2 brightness temperature mosaics from 2 February 2014 to 11 February 2014. Both data sets included 10 SAR mosaics and the corresponding daily AMSR-2 brightness temperature images.

The study period also ranged from 23 January 2014 to 11 February 2014. During this period the air temperature was varying quite much, the lowest hourly mean air temperatures during the test period at the Tankar coastal weather station (location 63.95^{o}N, 22.84^{o}E) were around -17 C^{o} and the highest around +3 C^{o}. The weather conditions during the training period were varying, there was a short cold period (1-2 days), then a warmer period and then colder again. During the test period, there were two warmer periods and one colder period (not as cold as the one short cold period during the training period with the lowest temperature of -17C^{o}). There were also cases of wet snow over the sea ice and dry snow over the sea ice during both the training and the test period.

We also performed tests for two of our test area image mosaics in the Kara and Barents Sea. In this Arctic test area the projection was polar stereographic with the WGS84 datum. The mid-longitude was 55 degrees (eastern) and the true scale latitude 70 degrees (northern). The latitudes in the area range from about 65°N to 85°N and longitudes from 0°E to 90°E. The ice and weather conditions in this Arctic area are different from the Baltic Sea. Typically the weather during the winter months is colder, usually clearly below zero degrees, and the snow cover is typically wet only during the melting period starting in May-June. Also in this Arctic test area the ice concentrations are varying because the ice is moving in most parts of the Arctic test area. Due to the colder temperatures less ice melting occur during the winter time. In the Baltic it is typical that some areas melt and re-freeze during the winter time due to rapid temperature changes.

5

3 Ice concentration estimation algorithm

3.1 SAR Processing

The SAR imagery were processed according to our standard procedure, first they were cali-
brated and rectified to Mercator projection, then an incidence angle correction was applied ac-
cording to (Makynen et al., 2002). After this daily SAR mosaics were computed by remapping
the SAR images into the study area such that newer data was always overlaid over older data,
producing mosaics with the newest SAR data at each mosaic grid cell or pixel. The resolution of
the SAR mosaics was 500 m. After this a segmentation step is performed for the daily mosaic.
Here we have used a Markov Random Field (MRF) based segmentation adapted from (Kato
et al., 1992; Berthod et al., 1996), but in practice any feasible segmentation, such as ICM (Iter-
ated Conditional Modes) (Besag, 1986) or even K-means (MacQueen, 1967) can be used with
rather similar results. The SAR segments with smaller size than 100 pixels (corresponding to an
area of $25\,km^2$) were combined to the adjacent larger segments with the closest HH backscat-
tering value (by an iterative process). The incidence angle correction has been designed for sea
ice and in general it does not work over the open water areas, where the SAR backscattering
is dependent on the water surface roughness i.e. waves. Wave conditions can change rapidly
depending on the winds and a good incidence angle correction over open water would require
reliable wave magnitude and direction information (i.e. 2-dimensional wave spectrum). Due to
the varying wave conditions the backscattering from open water in different SAR images can
vary significantly. This naturally can be seen in SAR mosaics and affects the SAR segmentation
in these areas. However, this effect is not a problem in e.g. concentration estimation or segment
classification as far as open water and segments with sea ice are separated by the segmentation.
We have tested our segmentation algorithm for SAR data of two whole Baltic Sea ice seasons
including all possible wind and temperature conditions, and according to our experience the
results are very reliable and large ice areas and large open water areas are separated almost in
every case. The possible errors may occur in warm conditions with very wet snow or water over
ice. And even in these cases we get reasonable ice concentration estimates for the segments pos-
sibly containing large areas of both open water and sea ice, but then we do not necessarily have

6

the information where within the (possible large) segment sea ice and open water (ice edge) are located. We have also studied of performing this segmentation using so-called principal component (PC) images of the two channels of dual-polarized SAR imagery. PC images consist of the first principal component computed of the two channels. According to our experience this has not improved the segmentation significantly in the sense that if we wish to separate between sea ice and open water i.e. have sea ice and open water in different segments, compared to visual interpretation. PC images, however improve the ice type segmentation in some cases (e.g. better distinguishing deformed ice). With a good incidence angle correction the SAR frame boundaries are not visible in the ice covered areas and the ice segments correspond to natural ice areas. Separating between natural open water segments is not possible because the wave conditions (surface roughness) are changing in much faster time scales) and backscattering, but on the other hand in our application we are not interested in classifying open water, e.g. based on surface roughness in more detail, but just locating open water segments and assigning zero ice concentration to these segments.

3.2 AMSR-2 processing

The AMSR-2 brightness temperature data were processed into daily mosaics similarly to SAR mosaicking, i.e. mosaics such that the new data was always written over older data. This data was presented in $10\,\mathrm{km}$ resolution. The brightness temperatures used in this study were from the $18.7\,\mathrm{GHz}$, $23.8\,\mathrm{GHz}$, $36.5\,\mathrm{GHz}$ and $89.0\,\mathrm{GHz}$, here denoted by $18\,\mathrm{GHz}$, $23\,\mathrm{GHz}$, $36\,\mathrm{GHz}$ and $89\,\mathrm{GHz}$ channels, respectively. All the AMSR-2 channels have both H and V polarizations. From the daily brightness temperature mosaic data all the polarization ratios (PR) and gradient ratios (GR) were derived according to the following equations:

$$\mathrm{PR}(f) = \frac{T_{\mathrm{B}}(f,V) - T_{\mathrm{B}}(f,H)}{T_{\mathrm{B}}(f,V) + T_{\mathrm{B}}(f,H)}, \tag{1}$$

and

$$\mathrm{GR}(f1,f2,p) = \frac{T_{\mathrm{B}}(f1,p) - T_{\mathrm{B}}(f2,p)}{T_{\mathrm{B}}(f1,p) + T_{\mathrm{B}}(f2,p)}. \tag{2}$$

7

By computing the polarization ratios for all the four frequencies, denoted by f, and the pairwise gradient ratios for all the four frequencies and for the two polarization, denoted by p, we get four polarization ratios and 12 gradient ratios at each grid cell. These are then used in the concentration estimation. The advantage of using polarization ratios is that they reduce the dependence on temperature, e.g. (Steffen et al., 1992). If the brightness temperatures were used, then also temperature estimates (e.g. from a numerical weather prediction model) or measurements at each grid point would be necessary for reliable ice concentration estimation.

A land mask, which was derived from the GSHHS coastline data (Wessel and Smith, 1996), was applied to the brightness temperatures in their original (low) resolution. Because mixed land-sea pixel complicate the computation they are either omitted or handled differently in the computation (Maass and Kaleschke, 2010). In this study the mixed land-sea pixels were omitted by our land masking. After this the brightness temperature values were extrapolated to cover a larger area overlapping the land areas, This technique was used to avoid re-sampling artifacts in the next phase and to guarantee a concentration estimate for each SAR segment. After this the brightness temperature grids were up-sampled to the SAR mosaic resolution (500 m) and a land masking in this high resolution was applied. This approach enables us to compute ice concentration estimates for the coastal SAR segments also.

We did not apply any explicit weather filtering. Typically weather filtering is based on ratios of channels sensitive to enhanced environment emission over open water. The NASA team. bootstrap ans ASI algorithms use the gradient ratios between 23.8GHz and 18.7 GHz, and 36.5 GHz and 18.7 GHz, respectively, in their weather filters. All these ratios are inputs to our neural network algorithm. If we assume that we have a representative training data set including enough samples of all the possible weather conditions, then the neural network should also be able to take the weather conditions into account. Our training data set only covered a relatively short period and was not representative in this sense, so it is expected that there may occur some estimation errors due to weather.

3.3 Combining brightness temperatures and SAR

After SAR segmentation we computed the mode of each polarization ratio and gradient ratio for each SAR segment. The mode was computed from up-sampled AMSR-2 polarization ratio and gradient ratio grids. Mode was selected as a metric because is is more robust with respect to outliers e.g. due to weather effects or variability in surface conditions. The concentration estimation for each SAR segment was based on these segment-wise modes of polarization and gradient ratios as MLP inputs. In this way we are able to produce an ice concentration estimate in the SAR mosaic resolution. The boundaries of different ice concentration areas corresponding to SAR segments are produced in the SAR resolution. Typically at the boundaries of ice and open water there are mixed ice/water pixels and the concentration estimates estimates at the edges are blurred. Using the SAR resolution reduces this blurring at the edges and produces sharper boundaries at the edges. Naturally the method is unable to extract smaller details than defined by the AMSR-2 resolution, but as concentration is a function of the resolution we still get reasonable concentration estimates over these areas also.

3.4 Concentration estimation

The ice concentration estimation is based on a MLP neural network. The neural network was trained using the error backpropagation algorithm (Haykin, 1999). The neural network was trained using the FMI gridded ice charts as its reference input. The hidden layer nonlinearities were implemented using the hyperbolic tangent (tanh) function. The single unit or artificial neuron of the output layer corresponding to the one MLP output (the estimated ice concentration) was linear. Feed-forward neural networks, such as MLP, with a single hidden layer of sigmoidal units are capable of approximating any continuous multivariate function, to any desired degree of accuracy (Hornik, 1989).

The output y_i of each MLP unit with index i is computed as

$$y_i = f_i \left(\sum_j W_{ij} y_j \right),$$ (3)

where f_i is the activation function of the unit (also known as a node or a neuron) i. At the hidden
5 layer the mapping is $f_i(x) = \tanh(x)$, and at the output layer the mapping is linear, i.e. $f_o(x) = x$. The weights W_{ij} are related to each input y_j, which are also outputs from the previous MLP
layer (or inputs at the input layer). In the training phase the outputs are first computed in the
forward direction and then the error is propagated back from the MLP output layer, i.e. starting
from the error between the ice concentration estimate given by the MLP and the desired ice
10 concentration defined by the training data, towards the input layer. A detailed derivation and
presentation of the error backpropagation learning rule can be found e.g. in Haykin (1999). In
our case the only output is the ice concentration, and thus our MLP has only one output unit.
In the training phase the weights W_{ij} are updated towards the negative gradient of the error
function at each node. To include a constant term (W_{k0}) also 1.0 is input into each MLP unit.
15 The used MLP architecture was 17-20-1, i.e. sixteen inputs corresponding to the four po-
larization ratios, 12 gradient ratios and the constant term (input 1.0), 20 hidden layer non-
linear units and one linear output layer unit, whose output is the ice concentration estimate.
A schematic diagram of the MLP used is shown in Fig. 2. The number of the hidden layer units
was determined experimentally: starting from two hidden-layer neurons and then iteratively
20 increasing the number of hidden-layer neurons, and performing the training until the training
error did not decrease notably any more by adding more hidden-layer neurons. Because the
algorithm makes the estimation segment-wise, not pixel-wise, the estimation is rather fast (in
practice it can be run for one mosaic image in a time range of a few seconds to a few tens of
seconds on a desktop personal computer, depending on the image and computing power of the
25 computer). We used the so-called epoch training, i.e. the whole training data set is iteratively
fed through the MLP in a random order, and each iteration corresponds to one epoch. In the
following equations the epochs are indicated by the time variable t, which is an integer number

starting from one. The learning rate parameter μ is adaptive. At the first epoch the learning rate is set to 0.005 and it is adjusted after each epoch t depending on the total MLP error E:

$$\mu(t+1) = 1.05\mu(t), \quad \text{if } E(t) < E(t-1), \tag{4}$$

$$\mu(t+1) = 0.70\mu(t), \quad \text{if } E(t) \geq E(t-1). \tag{5}$$

The number of training epochs used was 20 000. The MLP coefficients W_{ij} were initialized randomly, and the MLP coefficients corresponding to the minimum MLP total error E among 40 training runs were selected as the final MLP parameters, which are then used in the ice concentration estimation. This approach guarantees exclusion of a poor selection of the initial MLP weight coefficient configuration.

4 Evaluation

We evaluated the algorithm results by comparing them to the FMI digitized ice chart grids, which have a nominal resolution of 1 km, and to the high-resolution (3.125 km) UH ASI AMSR-2 algorithm (Beitsch et al., 2013; Beitsch and Kaleschke, 2014) results. We also made a visual comparison to the results of the AMSR-2 bootstrap algorithm ice concentrations provided by JAXA (Maeda, 2013; JAXA, 2013), which has a resolution of 10 km. The bootstrap algorithm uses the AMSR-2 channels of 36.5 GHz V (vertical) and 36.5 GHz H (horizontal), 18.7 GHz V, and 23.8 GHz V for weather filter. We also performed some comparisons over an Arctic Sea test area (Kara and Barents Seas), over which we make SAR mosaics daily. We used the same training data as used for the Baltic Sea, and the comparison to the AMSR-2 level 2 concentration results showed good agreement based on visual judgment: the high and low concentration areas in general corresponded to each other.

Comparison between SAR based ice concentration and reference data were made by using three error measures, L_1 error E_{L1}, the signed L_1 error E_{sgn} (describing the bias), and root

11

mean square (RMS) error E_{RMS}:

$$E_{L1} = \frac{1}{N_s} \sum_{i=1}^{N_s} \left| C_i^{\mathrm{est}} - C_i^{\mathrm{ref}} \right|, \tag{6}$$

$$E_{\mathrm{sgn}} = \frac{1}{N_s} \sum_{i=1}^{N_s} \left(C_i^{\mathrm{est}} - C_i^{\mathrm{ref}} \right). \tag{7}$$

$$E_{\mathrm{RMS}} = \sqrt{\frac{1}{N_s} \sum_{i=1}^{N_s} \left(C_i^{\mathrm{est}} - C_i^{\mathrm{ref}} \right)^2} \tag{8}$$

N_s is the number of pixels or grid cells computed over the whole ice concentration estimate grid area, C_i^{est} is the estimated concentration, and C_i^{ref} is the reference concentration at each pixel indicated by the index i. The error measures were computed over the SAR image mosaic area (with the grid cell spacing of 500 m), and the reference data were sampled into the same resolution by using bi-linear sampling. The comparisons were also grid cell based comparisons in the SAR mosaic resolution of 500 m. $E_{L1}(\geq 0)$ describes the mean absolute error, and E_{sgn} describes the bias or systematic error. If $E_{\mathrm{sgn}} < 0$, the algorithm underestimates, and if $E_{\mathrm{sgn}} > 0$, the algorithm overestimates the ice concentration compared to the reference data. RMS error represents the sample standard deviation of the differences between the estimated values and the reference values.

The comparison results can be seen in Table 1, the errors are given in percentage points. We also provide the standard deviations for the error measures, describing the variations between the images. For the training data set the ice concentration is slightly overestimated (2.95 percentage points) and for the test data set slightly underestimated (3.91 percentage points), the mean L_1 error for the training and test data sets is practically the same, about 8.7 percentage points. The standard deviations of the errors are relatively low for all the error measures indicating that the errors are quite similar for all the data. Two examples of the estimation result, the corresponding FMI ice chart concentrations, and the corresponding bootstrap algorithm concentration estimates can be seen in Figs. 3 and 4. In the SAR mosaic and segmentation result

12

(see Fig. 3) we can see that the open water areas produce different backscattering depending on the prevailing wave conditions and this can be seen as clear SAR frame boundaries in the open water areas of the SAR image mosaic and as many separate open water segments in the segmentation result. However, in the ice covered areas the SAR frame boundaries are not visible indicating that the incidence angle correction for sea ice has been successful. The ice edge has been sketched in the SAR mosaic of Fig. 3a as a red line, the ice covered area is in the northern/eastern side of the ice edge line. This indicates that the ice segments can be identified correctly over SAR frame boundaries in the mosaic, enabling computation of statistics and classification of the ice classes, and they are also separated from open water segments. In figures 3 and 4 we can for example see that the new algorithm is unable to capture parts of the ice-covered areas in the northern parts of Gulf of Finland (latitude around 60^oN). These areas are separated from open water by the SAR segmentation but as they are located near the coast, they are problematic for radiometer at a low resolution (mixed pixels) and for this reason the near-coast radiometer pixels are omitted. However, after this, to be able to assign a concentration estimate to each SAR segment, the radiometer brightness temperatures are extrapolated as described in Section 3.2. The estimates for the ice zones in the Gulf of Riga (located in southern part of the images, latitude around 58^oN, longitude 24^oE) corresponds the ice chart concentration much better than the bootstrap algorithm result in both cases of February 2 and February 11, presented in Figs. 3 and 4. Also for the February 11 case of Fig. 4 our algorithm gives high concentrations similar to the ice chart in the mid-parts of Gulf of Bothnia (northern parts of area, latitude about 63.5^oN, longitude about 20^oE). The bootstrap algorithm seems to underestimate the concentration in these areas. In Fig. 5 we can see a detail near the ice edge produced by our algorithm, the bootstrap algorithm and ASI algorithm. The different resolution of the different products can be seen in the details along the edge. In Figs. 6 and 7 we show the differences between the FMI ice chart and our algorithm result, and also a similar comparison to the UH ASI algorithm results. The ASI concentration estimates are also included in Figs. 3 and 4. This version utilizes the full resolution AMSR-2 data, and it can even capture the ice-covered zone in the northern Gulf of Finland. However, in the coastal zone the ASI algorithm seems to overestimate the ice concentration. This can be seen in both Figures 3 and 4 as non-zero

13

concentrations for example along the southern Swedish coast, where the other products or FMI ice charts do not indicate ice. Our new algorithm produces lower concentration estimates in the coastal zone. The largest differences between the FMI ice chart concentration and ASI concentration occur at the ice boundaries (ice edge), which have higher precision in FMI ice charts and also in our combined radiometer/SAR product. The numerical results of this comparison are given in Tables 2 and 3. We also performed this comparison in the ASI products resolution, and the error measures were 2.64, 10.80 and 22.95 percentage points for the signed error, L1 error and RMSE, respectively.

In some open water areas in the western parts of the Arctic test area mosaic over Kara and Barents Sea there occur some overestimations of the ice concentration, e.g. the open water area in the mid-left part of the image around an approximate coordinate location $(x,y)=(200,800)$. These are probably due to different weather conditions and open water signatures than in the Baltic Sea (training data set), and would also probably be corrected by including also data from the Arctic in the training phase. Arctic training data was not used in this study, because we did not have Arctic high-resolution ice chart concentrations available. The Arctic test was made just to see whether we can get reasonable results using the Baltic Sea training data. Also in the Arctic other data sources than ice charts must be used for training, these could be for example ASI or some other radiometer-based concentration results.

In general it can be said that the our algorithm results are slightly better than the ASI results compared to the FMI ice chart grids. This was an expectable result, because we have used FMI ice charts in training of our algorithm. The error measures for the ASI algorithm results compared to FMI ice chart grid results are some larger as shown in Tables 2 and 3.

Some comparisons between radiometer ice concentration products and other radiometer-based ice concentration products, visual ice concentration observation on-board a ship, e.g. in (Spreen et al., 2008) and visual/infrared (VIS/IR) earth-observation data, e.g. in (Cavalieri et al., 2006), have been made. The VIS/IR comparison require clear sky conditions or a reliable cloud mask. The correlation between the visual estimates and the ASI algorithm concentrations in (Spreen et al., 2008) were around 0.8 and in the inter-comparison between ASI, NASA team 2 algorithm and bootstrap algorithm the RMSE ranged from 7.2 to 10.8 and bias (signed error)

14

ranged from -2.0 to 1.7. All the compared algorithms used AMSR-E (Advanced Microwave Scanning Radiometer Earth Observing System) radiometer data as their input. In (Cavalieri et al., 2006) a comparison between Landsat-7 based ice concentrations and NASA Team-2 algorithm concentrations were made for some images and RMSE's were in the range 1-7, and
5 biases in the range 0-3. However, these results can not directly be compared to our error measures, because the comparisons have been made between different quantities.

The comparisons to the bootstrap ice concentrations provide by JAXA were visual evaluations of the differences. The results of our algorithm correspond to the results of the bootstrap algorithm quite well, based on visual general overview, but there are still some visible differ-
10 ences, especially in details due to different resolutions of the products. However, our algorithm also gives ice estimates over the coastal areas, and at the boundaries of different ice concentration zones are in the SAR mosaic resolution. The results of our algorithm and bootstrap ice concentrations are also seen in Figs. 3 and 4. We did not make numerical comparisons, because of the significantly different resolutions, in this case the effect of the resolution would proba-
15 bly had contributed more to the computed error than the actual error. Some rough estimates of the effect of the different resolutions to the concentration estimation error can be found e.g. in (Karvonen, 2014). To improve the performance more training data both from the Arctic and the Baltic Sea including different weather and ice conditions would be required to make a representative data set of the possible weather and ice conditions. Also studies on using the radiometer
20 data sampled to a higher resolution (similar to ASI) will be used to improve the algorithm performance in the future.

We also made a visual comparison for two ice concentration estimations over an Arctic ocean test area in the Barents and Kara Seas. Also in these areas the bootstrap algorithm concentrations and concentrations produced by our algorithm were in good agreement, as an example see
25 Fig. 8, even though the training was performed with a rather limited set of Baltic Sea data. We also compared our algorithm results to the ASI high-resolution results over this area for our two test images, the resulting difference map for the case shown in Fig. 8 is shown in Fig. 9. For this comparison we also give the error statistics in Table 2, but due to a very small Arctic data set these values are not very confident.

15

The did not find significant difference in performance of our algorithm and ASI algorithm in different concentration ranges, The error compared to FMI ice charts were similar, but in some cases the errors were made at different locations. The concentration distributions for our algorithm have less mid-range concentration values compared to bootstrap algorithm and ASI algorithm, the difference is larger for the bootstrap algorithm. This is due to the reduced blurring at the (open water and ice) edges. Because of its high resolution less edge blurring is generated by our algorithm.

5 Conclusion and discussion

conclusions

The comparison results to FMI ice charts were better than for example those reported for dual-polarized SAR data in (Karvonen, 2014). The best concentration estimates can very likely be achieved by combining SAR data and using radiometer data as a background value, such as has been done with the ice thickness values in (Karvonen et al., 2008), where modeled sea ice thickness is used as a background information and SAR imagery is used to improve the resolution of the estimates. The methodology may differ, but the basic idea is to enhance the background information based on SAR data to yield more precise estimates in a higher resolution compared to the background data resolution.

The training was performed using the polarization ratios and gradient ratios, because they provide a more stable basis for the ice concentration estimation with respect to the temperature changes. We also studied estimation by directly feeding the brightness temperatures into the MLP, but the MLP convergence was slower and estimation results worse with this approach. The reason for this behavior was obviously that to be able to also model the temperature dependence a representative training data set describing a wide range of temperature conditions would be required, and our training data set of ten day mosaics was too small for that purpose. However, it seems to be large enough when using ratios instead of brightness temperatures directly. We tested this by training our MLP with using the training data set brightness temperatures as inputs. The convergence of the algorithm was very slow (no good convergence even

after 100000 epochs), and after training of the MLP the estimation results even for the test set were poor, the mean errors were up to 40 percentage points for many image mosaicks. When using polarization and gradient ratios as inputs the convergence was faster and the error measures for the training data set reasonable. We believe even better results can be achieved by using an extensive representative training data set covering all possible ice types and weather conditions. However, already this experiment clearly indicates the potential of the methodology for providing high-resolution operational ice concentration estimates.

We have used the re-sampled AMSR-2 L1R (Level 1 Resampled) data having a resolution of about 10 km. We can see that the ASI algorithm utilizing the full AMSR-2 resolution (full resolution of the higher frequency channels) is capable of distinguishing details which are not all visible in the L1R data. It would be desirable to use the best possible resolution in the future operational algorithm and we are going to adapt our MLP algorithm to work with the high-precision data also, and after this high-resolution radiometer estimate we can still refine the segment boundaries based on SAR data to yield improved precision. Actually, all we need to do is to train the algorithm with suitably sampled high-resolution data for a representative training data set, after this it is capable of utilizing the full resolution.

The comparison results show that our algorithm estimates are closer to the FMI ice charts than the other two reference algorithms (bootstrap and ASI). This was an expected result, because the FMI ice charts are mainly based on visual interpretation of SAR data, and FMI ice charts and SAR data has been used in the training, and thus our algorithm has in a way been adapted to the FMI ice charts.

We were also surprised of the good estimation results in the Arctic test area, because the training data was from a relatively short period and from the Baltic Sea area. This can at least partly be explained by the fact that the in our Arctic test area there mainly exist only seasonal sea ice, only a little (less than one percent of the whole image area) multi-year can appear in the northeastern parts of the area. In areas with more multi-year ice the algorithm should be trained with similar data for reliable ice concentration estimates. Because in the Arctic we do not have digitized ice charts in our use, we should use other data sources for the training. One such data

source could be results of other radiometer ice concentration algorithms, like the bootstrap and ASI algorithms used as reference data here, refined by SAR imagery as presented in Sect. 3.3.

The advantage of the MLP approach is that it is not necessary to define parameters related to the brightness temperatures or ratios, all we need is a representative training data set to train the MLP. The disadvantage is that the actual nonlinear mapping from the input parameters to ice concentration remains unknown. The mapping is naturally described by the MLP weights and MLP structure, but the physical relationship between inputs and outputs remains unclear.

The novel method results to improved accuracy of the boundaries of the ice zones. As it can be seen the largest differences between our algorithm results and the reference products typically appear at the boundaries of the segments corresponding to the ice edge. This indicates that our algorithm is capable of representing the boundaries of regions with different concentration in a resolution defined by the SAR mosaic resolution. There still are some differences when comparing to ice chart concentrations, especially in the coastal zones. This can be explained by the low resolution of the radiometer data: in the case of a narrow ice zone near the coast the ice concentration is highly underestimated by our algorithm. This may be due to the narrow shape of the ice zone along the coastline, which are excluded by the land masking. These concentrations are better estimated by the 3 km ASI algorithm indicating that using higher resolution AMSR-2 data in our algorithm would also probably improve the estimation in the coastal areas. Also there seem to be some low-concentration areas produced by our algorithm in areas where the ice charts indicate much higher concentrations, For example the area in 3 approximately around (64^oN, 23^oE). It is very difficult to say whether these segments are due to the more precise distinguishing capability of the algorithm (when the ice analyst has given a concentration value for a larger polygon), or an estimation error (e.g. due to wet snow or water over the ice). In any case the use of segment-wise brightness temperature value modes seems to improve the ice concentration estimation significantly compared to radiometer data alone with respect to the gridded ice chart concentrations. It can be expected that applying our algorithm to radiometer data in a higher resolution the results would be even better, then the concentration of smaller ice areas and concentration areas near coasts would be estimated better.

18

References

references

Beitsch, A. and Kaleschke, L.: The February 2013 Arctic Sea Ice Fracture in the Beaufort Sea – a case study for two different AMSR2 sea ice concentration algorithms, Remote Sensing, accepted, 2014.

5　Beitsch, A., Kaleschke, L., and Kern, S.: AMSR2 ASI 3.125 km Sea Ice Concentration Data, V0.1, Institute of Oceanography, University of Hamburg, Germany, digital media (ftp://ftp-projects.zmaw. de/seaice/ (last access: 28 April 2014)),, 2013.

Berg, A.: Spaceborne SAR in Sea Ice Monitoring: Algorithm Development and Validation for the Baltic Sea, Licentiate thesis, Technical Report 47L, Chalmers University of Technology, Gothenburg, Swe-

10　den, 2011.

Berthod, M., Kato, Z., Yu, S., and Zerubia, J.: Bayesian image classification using Markov Random Fields, Image Vision Comput., 14, 285–295, 1996.

Besag, J.: On the statistical analysis of dirty pictures, J. Roy. Stat. Soc. B, 48, 259–302, 1986.

Bovith, T. and Andersen, S.: Sea Ice Concentration from Single-Polarized SAR data using Second-Order

15　Grey Level Statistics and Learning Vector Quantization, Scientific Report 05-04, Danish Meteorological Institute, Copenhagen, Denmark, 2005.

Cavalieri, D. J., Gloersen, P., and Campbell, W. J.: Determination of sea ice parameters with the NIMBUS 7 SMMR, J. Geophys. Res., 89, 5355–5369, 1984.

Cavalieri, D. J., Markus, T., Hall, D. K., Gasiewski, A. J., Klein, M., Ivanoff, A., Assessment of EOS

20　Aqua AMSR-E Arctic Sea Ice Concentrations Using Landsat-7 and Airborne Microwave Imagery, IEEE T. Geosci. Remote, 44(11), 3057–3069, 2006.

Clausi, D. A.: Comparison and fusion of co-occurrence, Gabor, and MRF texture features for classification of SAR sea ice imagery, Atmosphere and Oceans, 39, 183–194, 2001.

Clausi, D. A. and Jernigan, M. E.: Designing Gabor filters for optimal texture separability, Pattern

25　Recogn., 33, 1835–1849, 2000.

Comiso, J. C.: Characteristics of Arctic winter sea ice from satellite multispectral microwave observations, J. Geophys. Res., 91, 975–994, 1986.

Comiso, J. C.: SSM/I Sea Ice Concentrations Using the Bootstrap Algorithm, NASA Reference Publication / Goddard Space Flight Center 1380, Greenbelt, Maryland, USA., 1995.

30　Deng, H. and Clausi, D. A.: Gaussian MRF rotation-invariant features for image classification, IEEE T. Pattern Anal., 26, 951–955, 2004.

19

Deng, H. and Clausi, D. A.: Unsupervised segmentation of synthetic aperture radar sea ice imagery using a novel Markov random field model, IEEE T. Geosci. Remote, 43, 528–538, 2005.

Dokken, S. T., Hakansson, B., and Askne, J.: Inter-comparison of Arctic Sea ice concentration using RADARSAT, ERS, SSM/I and in-situ data, Can. J. Remote Sens., 26, 521–536, 2000.

Drüe, C. and Heinemann, G.: High-resolution maps of the sea-ice concentration from MODIS satellite data, Geophys. Res. Lett., 31, L20403, doi:http://dx.doi.org/10.1029/2004GL02080810.1029/2004GL020808, 2004.

Geldsetzer, T. and Yackel, J. J.: Sea ice type and open water discrimination using dual co-polarized C-band SAR, Can. J. Remote Sens., 35, 73–84, 2009.

Haralick, R. M., Shanmugam, K., and Dinstein, I.: Textural features for image classification, IEEE T. Syst. Man Cyb., SMC-3, 610–621, 1973.

Haykin, S. S.: Neural Networks, a Comprehensive Foundation, 2nd edn., Prentice Hall, Upper Saddle River, N.J., USA., 183–196, 1999.

Hornik, K., Stinchcombe, M., and White, H.: Multilayer feedforward networks are universal approximators, Neural Networks, 2, 359–366, 1989.

JAXA: Descriptions of GCOM-W1 AMSR2 Level 1R and Level 2 Algorithms, Rev.A, available at: http://suzaku.eorc.jaxa.jp/GCOM_W/data/data_w_algorithm.html (last access: 28 April 2014), 2013.

Kaleschke, L. and Kern, S.: ERS-2 SAR Image Analysis for Sea Ice Classification in the Marginal Ice Zone, Proc. IEEE International geoscience and remote sensing symposium 2000 (IGARSS 2000), V, 3038–3040, July 24-28, 2000, Honolulu, Hawaii, USA., 2000.

Kaleschke, L., Lupkes, C., Vihma, T., Haarpaintner, J., Bochert, A., Hartmann, J., and Heygster, G.: SSM/I sea ice remote sensing for mesoscale ocean-atmosphere interaction analysis, Can. J. Remote Sens., 27, 526–537, 2001.

Karvonen, J.: Baltic Sea ice concentration estimation based on C-Band HH-Polarized SAR data, IEEE J. Sel. Top. Appl., 5, 1874–1884, doi:http://dx.doi.org/10.1109/JSTARS.2012.220919910.1109/JSTARS.2012.2209199, 2012.

Karvonen, J.: Baltic Sea ice concentration estimation based on C-Band Dual-Polarized SAR data, IEEE T. Geosci. Remote, doi:http://dx.doi.org/10.1109/TGRS.2013.229033110.1109/TGRS.2013.2290331, to be published, 2014.

Karvonen, J., Simila, M., and Makynen, M.: Open water detection from Baltic Sea Ice Radarsat-1 SAR imagery, IEEE Geosci. Remote S, 2, 275–279, 2005.

20

Karvonen, J., Cheng, B., and Simila, M.: Ice Thickness Charts Produced by C-Band SAR Imagery and HIGHTSI Thermodynamic Ice Model, Proc. of the Sixth Workshop on Baltic Sea Ice Climate, 71–81, 25–28 August 2008, Lammi, Finland 2008.

Karvonen, J., Cheng, B., Vihma, T., Arkett, M., and Carrieres, T.: A method for sea ice thickness and concentration analysis based on SAR data and a thermodynamic model, The Cryosphere, 6, 1507–1526, doi:http://dx.doi.org/10.5194/tc-6-1507-201210.5194/tc-6-1507-2012, 2012.

Kato, Z., Zerubia, J., and Berthod, M.: Satellite Image Classification Using a Modified Metropolis Dynamics, in: Proceedings of IEEE International Conference on Acoustics, Speech and Signal Processing (ICASSP 92), 3, 23–26 March 1992, San Francisco, California, USA, 573–576, March, 1992.

Kern, S.: A new algorithm to retrieve the sea ice concentration using weather-corrected 85 GHz SSM/I measurements, Ph.D. thesis, Dept. Physics Elect. Eng., Univ. Bremen, Bremen, Germany, 2001.

Kern, S. and Heygster, G.: Sea-ice concentration retrieval in the antarctic based on the SSM/I 85.5 GHz polarization, Ann. Glaciol., 33, 109–114, 2001.

Kern, S., Kaleschke, L., and Clausi, D. A.: A comparison of two 85-GHz SSM/I ice concentration algorithms with AVHRR and ERS-2 SAR imagery, IEEE T. Geosci. Remote, 41, 2294–2306, 2002.

Leigh, S., Wang, Z., and Clausi, D. A.: Automated ice-water classification using dual polarization SAR satellite imagery, IEEE T. Geosci. Remote, 52, 5529–5539, 2014.

MacQueen, J. B.: Some Methods for classification and Analysis of Multivariate Observations, in: Proceedings of 5th Berkeley Symposium on Mathematical Statistics and Probability, 21 June 21–18 July 1965 and 27 December 1965–7 June 1966, University of California Press., 281–297, 1967.

Maeda, T.: AMSR2 L1R Product, JAXA, available at: http://suzaku.eorc.jaxa.jp/GCOM_W/materials/product/AMSR2_L1R.pdf (last access: 28 April 2014), 2013.

Maillard, P., Clausi, D. A., and Deng, H.: Map-guided sea ice segmentation and classification using SAR imagery and a MRF segmentation scheme, IEEE T. Geosci. Remote, 43, 2940–2951, 2005.

Makynen, M., Manninen, T., Simila, M., Karvonen, J., and Hallikainen, M.: Incidence angle dependence of the statistical properties of the C-Band HH-Polarization backscattering signatures of the Baltic Sea Ice, IEEE T. Geosci. Remote, 40, 2593–2605, 2002.

Maass N,. Kaleschke L.: Improving passive microwave sea ice concentration algorithms for coastal areas: applications to the Baltic Sea, Tellus, 62A, 393–410, 2010.

Ochilov, S. and Clausi, D. A.: Operational SAR sea-ice classification, IEEE T. Geosci. Remote, 50, 4397–4408, 2012.

Pichler, O., Teuner, A. S., and Hosticka, B. J.: A comparison of texture feature extraction using adaptive gabor filtering, pyramidal and tree structured wavelet transforms, Pattern Recogn., 29, 733–742, 1996.

21

Rue, H. and Held, L.: Gaussian Markov Random Fields: Theory and Applications, CRC Press, 2005.

Spreen, G., Kaleschke, L., and Heygster, G.: Sea ice remote sensing using AMSR-E 89-GHz channels, J. Geophys. Res., 113, C02S03, doi:http://dx.doi.org/10.1029/2005JC00338410.1029/2005JC003384, 2008.

Steffen, K., Key, J., Cavalieri, D. J., Comiso, J., Gloersen, P., St. Germain, K., and Rubinstein, I.: The estimation of geophysical parameters using passive microwave algorithms, Ch. 10, in: Microwave Remote Sensing of Sea Ice, edited by: Carsey, F. D., American Geophysical Society/Wiley, Washington D.C., USA., 201–231, 1992.

Yu, Q. and Clausi, D. A.: SAR sea-ice image analysis based on iterative region growing using semantics, IEEE T. Geosci. Remote, 45, 3919–3931, 2007.

Wessel, P. and Smith, W. H. F.: A global self-consistent, hierarchical, high-resolution shoreline database, J. Geophys. Res., 101, 8741–8743, 1996.

Table 1. Errors for our algorithm results compared to FMI ice charts for the training and test data sets. The latitude range of the area is from 56 to 66 degrees (north), and longitude range from 16 to 31 degrees (eastern), the results were computed for data rectified to Mercator projection with a resolution of 500m. For both the data sets (training and test sets) the number of scenes $N = 10$.

table

Measure	Signed error	L1 error	RMSE
Training data set			
Error	2.95	8.67	19.98
Std. dev.	3.33	2.02	2.42
Test data set			
Error	−3.91	8.66	21.28
Std. dev.	2.67	1.98	3.29

Table 2. Errors for our algorithm results compared to ASI ice concentrations for the test data set, and for two Arctic ocean cases (corresponding to two daily SAR mosaics). The results were computed for data rectified to polar stereographic projection with a resolution of 500m.

Measure	Signed error	L1 error	RMSE
Test data set (Baltic)			
Error	−1.23	11.15	25.19
Std. dev.	7.84	4.15	5.35
Arctic ocean test cases			
Error	−3.29	6.68	16.85
Std. dev.	5.56	4.20	5.98

Table 3. Errors for the comparison between FMI ice charts and the ASI results. The same Mercator projection as in other Baltic Sea comparisons was used.

Measure	Signed error	L1 error	RMSE
Test data set (Baltic)			
Error	5.38	11.81	27.30
Std. dev.	4.31	2.54	3.28
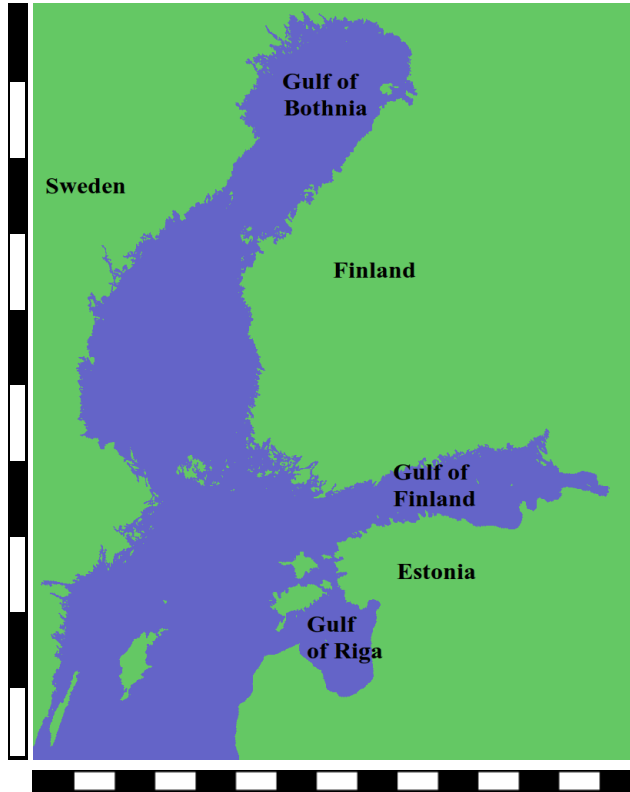
Fig. 1. The Baltic Sea study area. In the image scales the interval is one degree in both latitude and longitude, the upper left corner is (66°N,16°E) and lower right corner (56°N,31°E).
figure
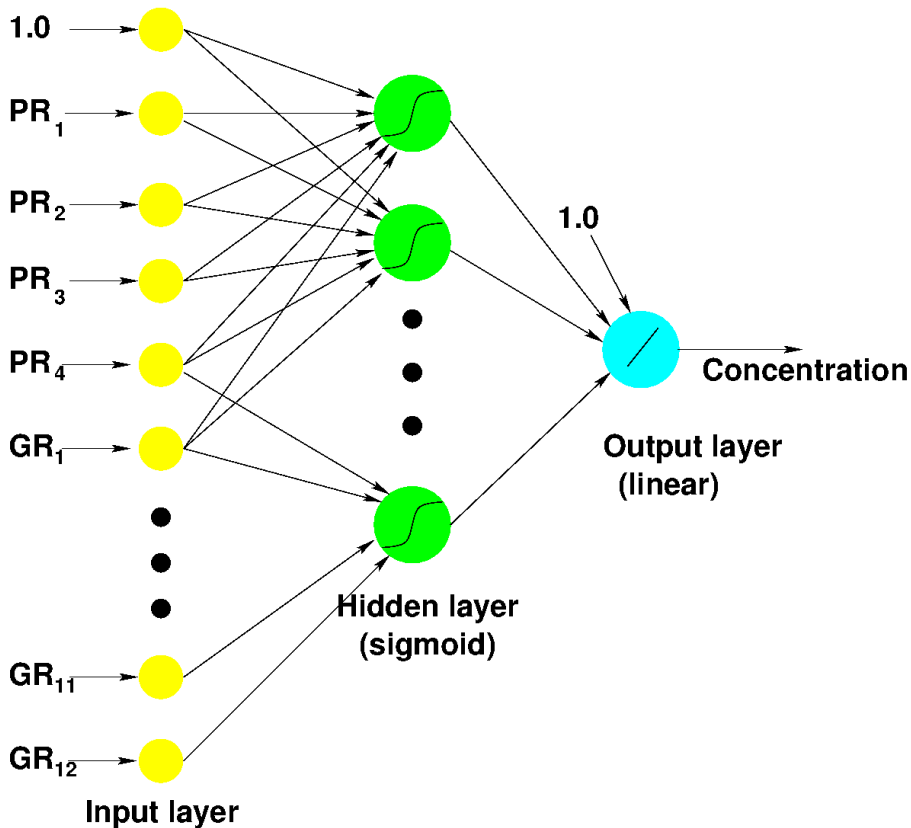
Fig. 2. A schematic diagram of the MLP architecture used, there are 17 input layer units (including the constant term 1.0, 20 hidden layer sigmoid units, and one linear output layer unit. For clarity not all the connection have been drawn in the figure.
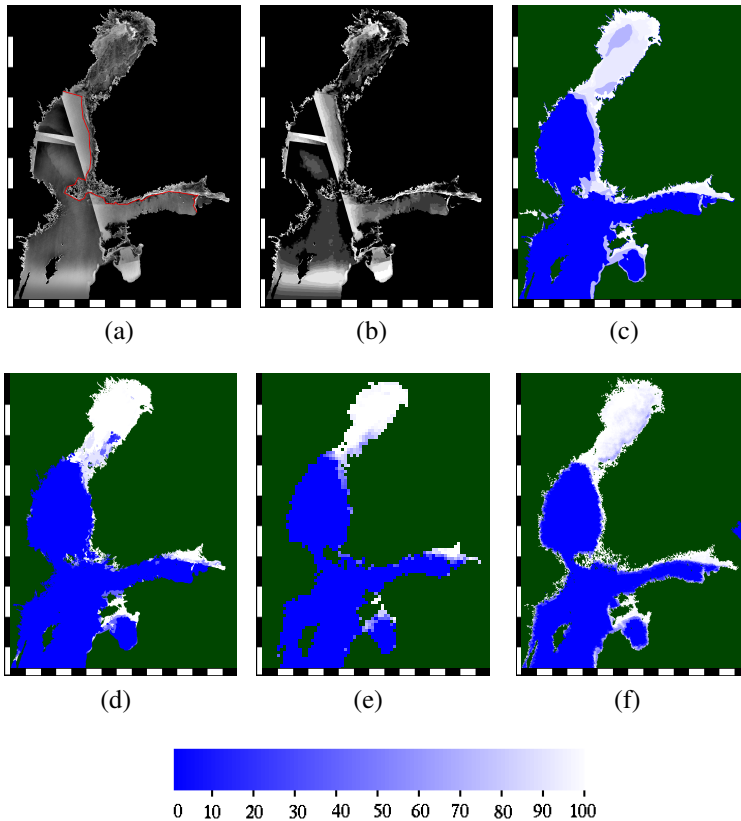
Fig. 3. SAR image mosaic of Feb. 2, 2014, ©MDA (a), the ice edge has been indicated by the red line, segmentation result (b), FMI ice chart grid ice concentration (c),ice concentration estimate using our algorithm (d), AMSR-2 bootstrap algorithm ice concentration give in 10km resolution (e), ASI ice concentration (f). In the image scales the interval is one degree in both latitude and longitude, the upper left corner is (66^oN,16^oE) and lower right corner (56^oN,31^oE).

28
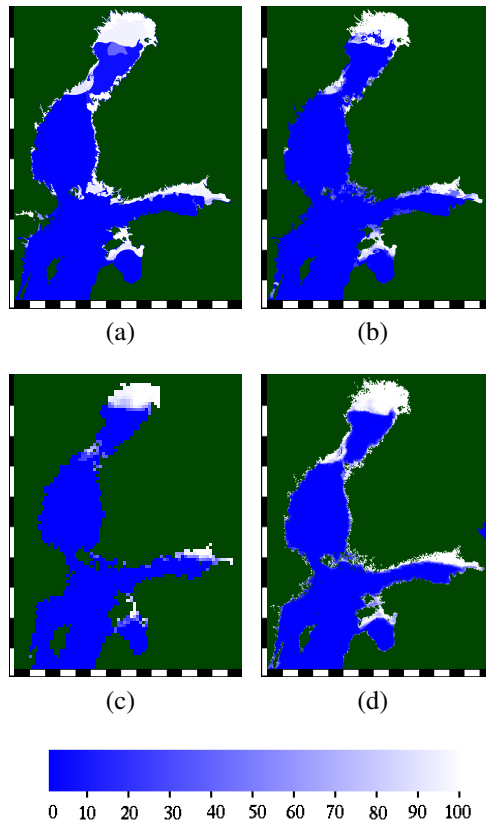
Fig. 4. FMI ice chart concentration grid for Feb. 11, 2014 (a), ice concentration estimate using our algorithm (b), AMSR-2 bootstrap algorithm ice concentration (c), and ASI ice concentration (d). In the image scales the interval is one degree in both latitude and longitude, the upper left corner is (66°N,16°E) and lower right corner (56°N,31°E).
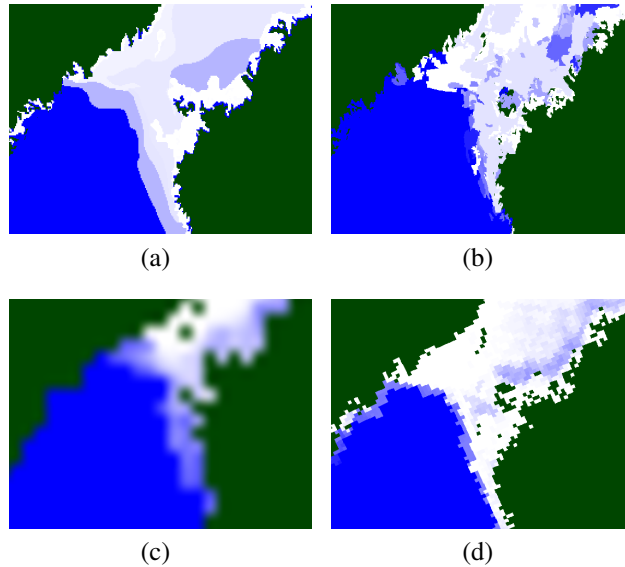
Fig. 5. A detail of the Feb. 2, 2014 concentration estimates near the ice edge. FMI ice chart concentration (a), our algorithm result (b), bootstrap ice concentration (c), and ASI concentration (d). In the image scales the interval is one degree in both latitude and longitude, the upper left corner is (66^oN,16^oE) and lower right corner (56^oN,31^oE).
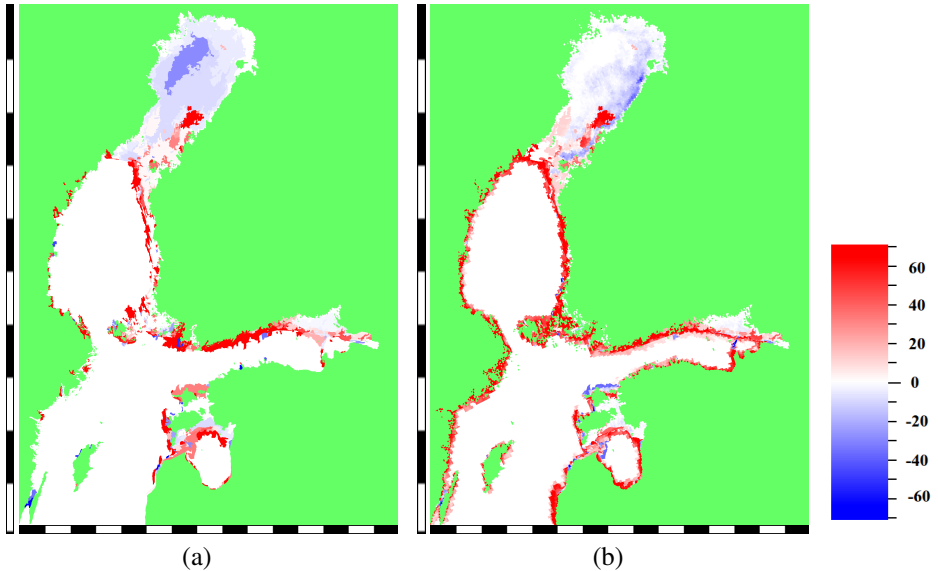
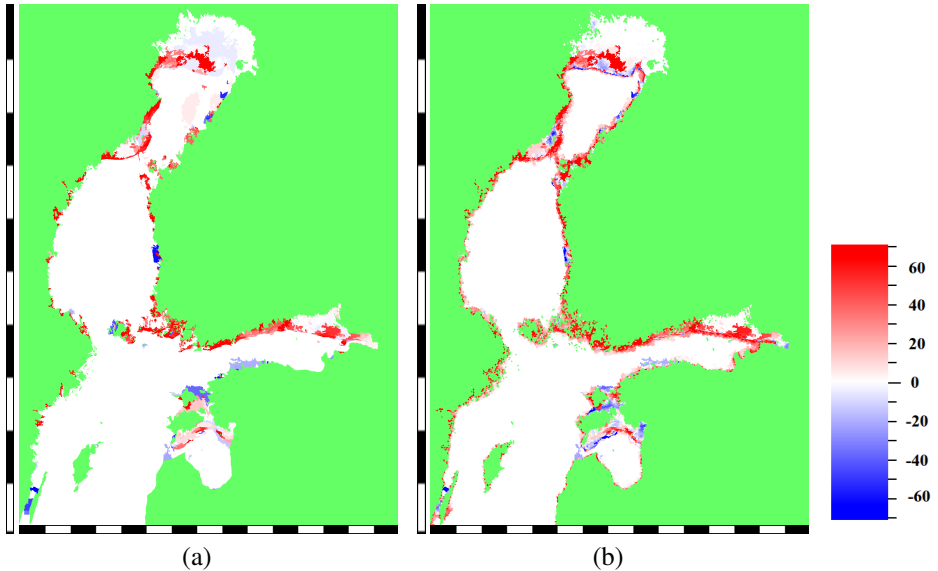**Fig. 6.** Difference between the algorithm result and FMI ice chart concentration for Feb 2, 2014 (a), and between the algorithm result and ASI concentration (b). Overestimation produced by our algorithm with respect to the reference data is indicated by the blue tones (negative difference values) and underestimation by red (positive values). In the image scales the interval is one degree in both latitude and longitude, the upper left corner is (66°N,16°E) and lower right corner (56°N,31°E).

Fig. 7. Difference between our algorithm result and FMI ice chart concentration for Feb 11, 2014 (a), and between the our result and ASI concentration (b). Overestimation produced by our algorithm with respect to the reference data is indicated by the blue tones (negative difference values) and underestimation by red (positive values). In the image scales the interval is one degree in both latitude and longitude, the upper left corner is (66^oN,16^oE) and lower right corner (56^oN,31^oE).
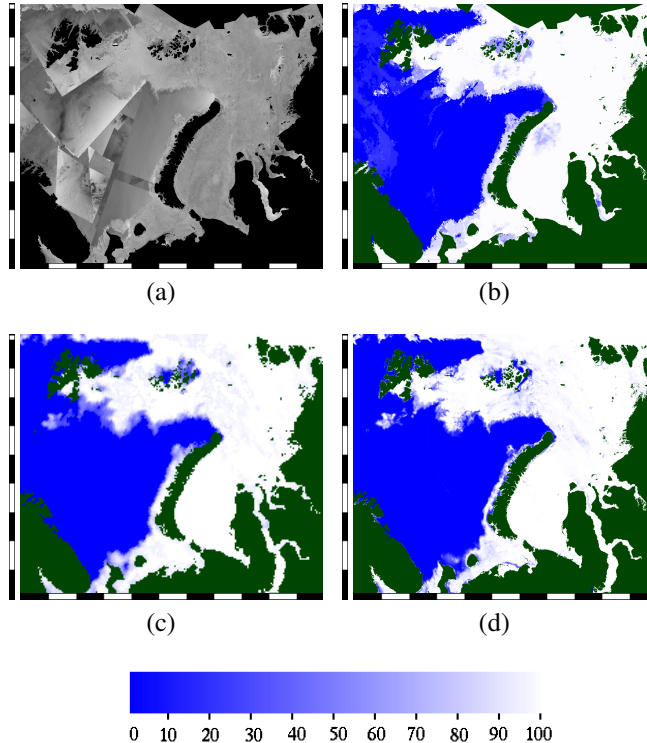
Fig. 8. An example of the Arctic ocean ice concentration estimation, the SAR mosaic of Feb 2, 2014 (a), ice concentration estimate based on our algorithm (b), the AMSR-2 level 2 ice concentration product (c), and ASI ice concentration product (d). Some parts of the area are not covered by the SAR mosaic (indicated by black tone, such as the land mask, in the mosaick image) and the concentration of our product is only given in the area of the SAR mosaic cover. The image scale interval is 200km, the whole image size is 2200km (x-direction, vertical) and 1850km (y-direction, horizontal). The origin of the coordinate system referred in the text is at the lower left corner.
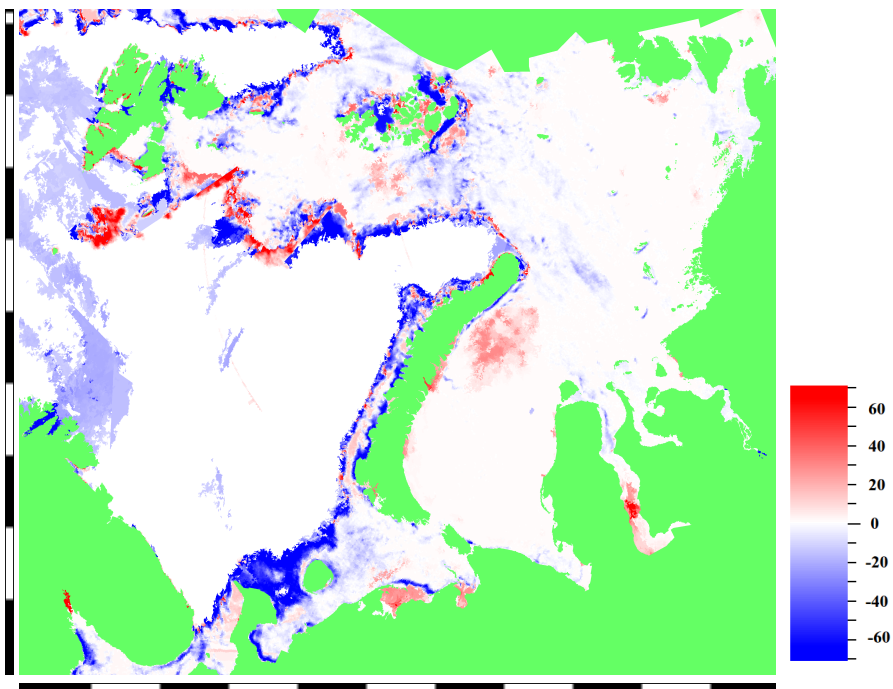
Fig. 9. The difference between the FMI algorithm concentration and ASI ice concentration for the Arctic study area, Feb 2, 2014. The values in the areas where our algorithm indicates higher concentration than ASI appear as blue and areas where our algorithm indicates lower concentration appear as red. The image scale interval is 200km, the whole image size is 2200km (x-direction, vertical) and 1850km (y-direction, horizontal).